

Hidden antiferro-nematic order in Fe-based superconductor BaFe₂As₂ and NaFeAs above T_S

Seiichiro Onari and Hiroshi Kontani

Department of Physics, Nagoya University, Furo-cho, Nagoya 464-8602, Japan.

(Dated: November 2, 2020)

In several Fe-based superconductors, slight C_4 symmetry breaking occurs at T^* , which is tens of Kelvin higher than the structural transition temperature T_S . In this “hidden” nematic state at $T_S < T < T^*$, the orthorhombicity is tiny [$\phi = (a - b)/(a + b) \ll 0.1\%$], but clear evidences of bulk phase transition have been accumulated. To explain this long-standing mystery, we propose the emergence of antiferro-bond (AFB) order with the antiferro wavevector $\mathbf{q} = (0, \pi)$ at $T = T^*$, by which the characteristic phenomena below T^* are satisfactorily explained. This AFB order originates from the inter-orbital nesting between the d_{xy} -orbital hole-pocket and the electron-pocket, and this inter-orbital bond order naturally explains the pseudogap, band-folding, and tiny nematicity that is linear in $T^* - T$. The hidden AFB order explains key experiments in both BaFe₂As₂ and NaFeAs, but it is not expected to occur in FeSe because of the absence of the d_{xy} -orbital hole-pocket.

The emergence of rich nematic phase transitions is a central unsolved issue in Fe-based superconductors. At the structural transition temperature T_S , ferro-orbital (FO) order with $\psi \equiv (n_{xz} - n_{yz})/(n_{xz} + n_{yz}) \neq 0$ is driven by electron correlation [1], by which the orthorhombicity $\phi = (a - b)/(a + b)$ occurs in proportion to ψ . Above T_S , the electronic nematic susceptibility develops divergently [2–5]. As possible mechanisms of nematicity, both spin-nematic scenarios [6–12] and the orbital/charge-order scenarios [13–24] have been proposed. Both scenarios were successfully applied to the nematicity in BaTi₂Sb₂O [25–27] and cuprate superconductors [28].

However, the nematicity in Fe-based superconductors recently exhibits very rich variety beyond the original expectation. Well-known discoveries are the nematicity without magnetization in FeSe and the nematicity with B_{2g} symmetry in the heavily hole-doped compound AFe₂As₂ (A=Cs, Rb) [29–33], which is rotated by 45° with respect to the nematicity in FeSe. These nematic orders are naturally understood as the ferro orbital and/or bond orders driven by the interference between spin fluctuations described in Fig. 1(a) [17], where $C_{\mathbf{Q}_s, \mathbf{Q}'_s}$ gives the three-boson coupling.

The most significant open issue in the nematicity is the emergence of another type of nematicity in various Ba122 compounds below $T = T^*$, which is higher than T_S by tens of Kelvin. A true second-order bulk nematic transition at T^* has been reported in many experimental studies, such as a magnetic torque study [34], an X-ray study [35], an optical measurement study [36], and a laser photoemission electron microscope study [37].

Below T^* , the orthorhombicity ϕ is finite but very small ($\ll 0.1\%$), but a sizable pseudogap and shadow band exist [38, 39]. The exponent of the nematicity $\psi \propto \phi \propto (T^* - T)^\alpha$ is $\alpha \sim 1$, which is much larger than the mean-field exponent (1/2). The relation $\phi \propto (T^* - T)$ is also observed in NaFeAs [40]. One may consider that the nematicity at T^* is not a true phase transition but that it reflects the inhomogeneity of the FO-order tran-

sition temperature T_S due to local uniaxial pressure and randomness [7, 41, 42]. On the other hand, T^* seems not to be sensitive to the sample quality, and the domain structure of nematicity observed in the C_4 phase above T_S [36, 37] is homogeneous. The aim of this study is to reveal the origin of this mysterious hidden nematic state below $T = T^*$ and to explain why multistage-nematic transitions (at $T = T^*$ and T_S) emerge in Ba122 and NaFeAs families.

In this paper, we predict the emergence of antiferro-bond (AFB) order with the antiferro wavevector $\mathbf{q} = (0, \pi)$ at $T = T^*$ above the FO-order transition temperature T_S . Below T^* , the AFB order causes a pseudogap in the density of states and the small T -linear nematicity $\psi \propto T^* - T$. The AFB order does not interrupt the ferro-orbital order at T_S , because these order parameters have different orbital components. Thus, both the spin and nematic susceptibilities, $\chi^s(\mathbf{Q})$ and $\chi_{\text{nem}}(\mathbf{0})$ respectively, show only a small anomaly at $T = T^*$. The obtained inter-orbital AFB order is driven by the interference between antiferro and ferro spin fluctuations, which are caused by the inter-orbital nesting between the d_{xy} -orbital hole-pocket and electron pockets. The present theory naturally explains the long-standing mystery of the hidden nematic state below T^* in Ba122 and NaFeAs families, in both of which T -linear nematicity has been reported [34, 40].

In contrast, the AFB order does not occur in the FeSe model that has no d_{xy} -orbital hole-pocket, since the inter-orbital nesting is essential to realize the AFB order. This result is consistent with the absence of T^* in FeSe [43].

Below, we denote the five d -orbitals $d_{3z^2-r^2}$, d_{xz} , d_{yz} , d_{xy} , and $d_{x^2-y^2}$ as $l = 1, 2, 3, 4$, and 5, respectively. We analyze the following two-dimensional eight-orbital d - p Hubbard model with parameter r [19]:

$$H_M(r) = H^0 + rH^U, \quad (1)$$

where H^0 is the unfolded tight-binding model for BaFe₂As₂ [44], FeSe [19], and NaFeAs; more details are

presented in Supplementary Material (SM) A [45]. H^U is the first-principles screened d -electron Coulomb potential in each compound [46], and r is the reduction parameter, which is approximately proportional to the renormalization factor z in the coherence part of the Green function [20]. We note that r is the unique free parameter in the present theory. We set r to reproduce experimental weak (FeSe) or moderate (NaFeAs, BaFe₂As₂) spin fluctuation strength in the RPA.

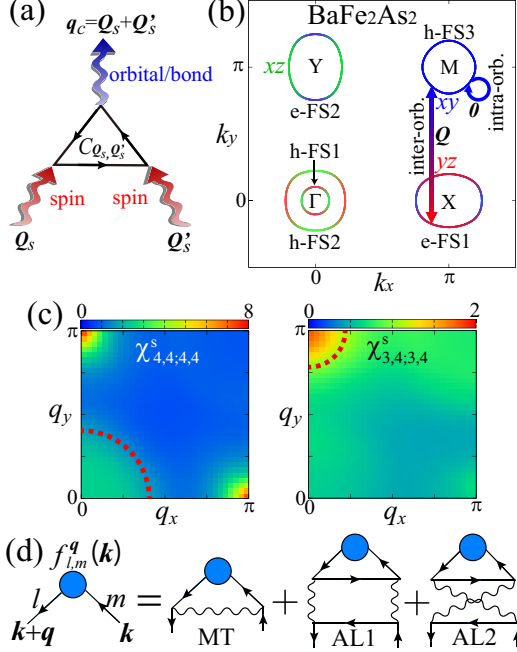


FIG. 1. (a) Quantum process of the spin-fluctuation-driven orbital fluctuations with $\mathbf{q}_c = \mathbf{Q}_s + \mathbf{Q}'_s$. (b) FSs of the BaFe₂As₂ model in the unfolded zone. The colors green, red and blue correspond to orbitals 2, 3, and 4, respectively. (c) \mathbf{q} dependences of $\chi_{4,4;4,4}^s(\mathbf{q}, 0)$ and $\chi_{3,4;3,4}^s(\mathbf{q}, 0)$ given by the RPA. The large antiferro- and ferro-fluctuations shown by dotted circles are significant for the AFB order formation. (d) Feynman diagrams of the DW equation. Each wavy line represents a fluctuation-mediated interaction.

First, we focus on the unfolded BaFe₂As₂ model directly given by the first-principles calculation using WIEN2k. Figure 1(b) shows the unfolded Fermi surfaces (FSs). The size of h-FS3 around M point composed of orbital 4 is similar to that of e-FS1(2) around X(Y) point, which results in a good inter-orbital nesting. We calculate the spin (charge) susceptibilities $\hat{\chi}^{s(c)}(\mathbf{q})$ for $\mathbf{q} = (\mathbf{q}, \omega_m = 2m\pi T)$ based on the random-phase-approximation (RPA). The spin Stoner factor α_s is defined as the maximum eigenvalue of $\hat{\Gamma}^s \hat{\chi}^0(\mathbf{q}, 0)$, where $\hat{\Gamma}^{s(c)}$ is the bare Coulomb interaction for the spin (charge) channel, and $\hat{\chi}^0$ is the irreducible susceptibilities given by the Green function without self-energy $\hat{G}(\mathbf{k}) = [(i\epsilon_n - \mu)\hat{1} - \hat{h}^0(\mathbf{k})]^{-1}$ for $\mathbf{k} = [\mathbf{k}, \epsilon_n = (2n+1)\pi T]$. Since the relation $\hat{\chi}^s(\mathbf{q}) \propto \frac{1}{1-\alpha_s}$ holds, spin fluctuations become large

with increasing α_s ($\propto r$), and $\alpha_s = 1$ corresponds to spin-ordered state. Here, $\hat{h}^0(\mathbf{k})$ is the matrix expression of H^0 and μ is the chemical potential. Details of $\hat{\Gamma}^{s(c)}$, $\hat{\chi}^{s(c)}(\mathbf{q})$, and $\hat{\chi}^0(\mathbf{q})$ are presented in SM A [45]. We fix the parameters $r = 0.303$ in the BaFe₂As₂ model unless otherwise noted. In this case, $\alpha_s = 0.96$ at $T = 30\text{meV}$, and the averaged intra-orbital Coulomb interaction is $rU \sim 1.6\text{eV}$. Figure 1(c) shows the obtained spin susceptibilities $\chi_{4,4;4,4}^s(\mathbf{q}, 0)$ and $\chi_{3,4;3,4}^s(\mathbf{q}, 0)$, the peaks of which at $\mathbf{q} = (0, \pi)$ originate from the intra-orbital (4-4) and the inter-orbital (3-4) nesting, respectively. $\chi_{4,4;4,4}^s$ is larger than $\chi_{3,4;3,4}^s$ because of the good intra- d_{xy} -orbital nesting between e-FSs and h-FS3.

Hereafter, we study the symmetry breaking in the self-energy $\hat{f}^{\mathbf{q}}$ for wavevector \mathbf{q} based on the density-wave (DW) equation introduced in Ref. [19, 32, 47]. We calculate both the momentum and orbital dependences of \hat{f} self-consistently to analyze both the orbital order and bond order on equal footing. To identify the realized DW with wavevector \mathbf{q} , we solve the linearized DW equation:

$$\lambda_{\mathbf{q}} f_{l,l'}^{\mathbf{q}}(k) = \frac{T}{N} \sum_{k', m, m'} K_{l,l'; m, m'}^{\mathbf{q}}(k, k') f_{m, m'}^{\mathbf{q}}(k'), \quad (2)$$

where $\lambda_{\mathbf{q}}$ is the eigenvalue of the DW equation. The DW with wavevector \mathbf{q} appears when $\lambda_{\mathbf{q}} = 1$, and the eigenvector $\hat{f}^{\mathbf{q}}(k)$ gives the DW form factor. A larger value of $\lambda_{\mathbf{q}}$ corresponds to a more dominant DW state. Details of the kernel function $\hat{K}^{\mathbf{q}}(k, k')$ are given in SM A [45]. The Maki-Thompson (MT) terms and Aslamazov-Larkin (AL) terms shown in Fig. 1(d) are included in the kernel function. Near the magnetic criticality, the AL terms are strongly enhanced in proportion to $\sum_p \chi^s(p) \chi^s(-p + \mathbf{q}_c)$, and they induce charge DW order through the three-boson coupling C_{Q_s, Q'_s} in Fig. 1(a).

Figure 2(a) shows the \mathbf{q} -dependences of $\lambda_{\mathbf{q}}$ for the total terms, the MT terms, and AL terms at $T = 32.4\text{meV}$. $\mathbf{q} = (0, \pi)$ AFB order appears at $T^* = 32.4\text{meV}$, while $\lambda_{\mathbf{0}}$ is slightly smaller than unity. Thus, the ferro-orbital transition temperature T_S is lower than T^* . The relation $\lambda_{(0, \pi)} > \lambda_{\mathbf{0}}$ is robust in the presence of moderate spin fluctuations $\alpha_s \gtrsim 0.85$. Both the AL and MT terms contribute to the AFB order cooperatively as shown in Fig. 2(a). Figure 2(b) shows the dominant component of the static form factor, $f_{3,4}^{\mathbf{q}}(\mathbf{k})$, for $\mathbf{q} = (0, \pi)$, which is derived from the analytic continuation of $\hat{f}^{\mathbf{q}}(k)$. The other sub-dominant components are explained in SM B [45]. Focusing on the X and M points, $f_{3,4}^{(0, \pi)}(\mathbf{k})$ is proportional to $-\cos(k_y)$, which corresponds to the inter-orbital AFB order shown in Fig. 2(c), where the y -direction hoppings between orbitals 3 and 4 are modulated by the correlation hopping $\delta t_{3,4}(y; y \pm 1) = -\delta t_{4,3}(y; y \pm 1) = \delta t(-1)^y$. Note that $\delta t_{l,m}(y; y')$ is real and equal to $\delta t_{m,l}(y'; y)$.

The origin of the AFB order $f_{3,4}^{(0, \pi)}$ is the quantum interference between the antiferro-spin fluctuations $\chi_{3,4;3,4}^s(\mathbf{Q})$ for $\mathbf{Q} \approx (0, \pi)$ and ferro-spin fluctuations

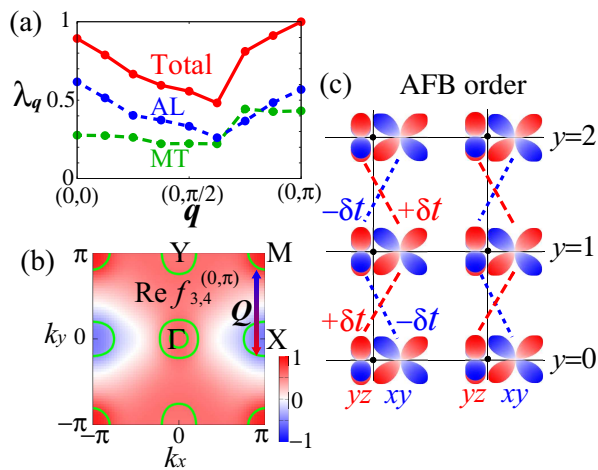


FIG. 2. (a) Obtained \mathbf{q} dependences of $\lambda_{\mathbf{q}}$ at $T = 32.4\text{meV}$. The contributions from the AL and MT terms are also shown. (b) Dominant component of the form factor at $\mathbf{q} = (0, \pi)$, $f_{3,4}^{\mathbf{q}}(\mathbf{k})$, which is given by the off-diagonal orbitals 3 and 4. The green lines indicate FSS. (c) Picture of the inter-orbital AFB order induced by $f_{3,4}^{(0,\pi)}$.

$\chi_{4,4;4,4}^s(\mathbf{0})$ shown in Fig. 1(a). The former is enhanced by the inter-orbital nesting shown in Fig. 1(b), while the latter $\chi_{4,4;4,4}^s(\mathbf{0})$ is caused moderately by the forward intra-orbital scattering of orbital 4 in h-FS3. The developments of $\chi_{3,4;3,4}^s(\mathbf{Q})$ and $\chi_{4,4;4,4}^s(\mathbf{0})$ are shown by the red dotted circle in Fig. 1(c). Moreover, the three-boson coupling $C_{\mathbf{Q}_s, \mathbf{Q}'_s}$ in Fig. 1(a) is strongly enlarged when $\mathbf{q}_c = \mathbf{Q}_s + \mathbf{Q}'_s$ is a nesting vector [48], and this condition is satisfied when $\mathbf{Q}_s = \mathbf{Q}$ and $\mathbf{Q}'_s = \mathbf{0}$. Thus, $\lambda_{\mathbf{Q}}$ becomes large due to the AL terms. In addition to the AL terms, the MT terms strengthen the sign change of $f_{3,4}^{(0,\pi)}(\mathbf{k})$ between X and M points, as reported previously [19, 32, 49]. Thus, the AFB order originates from the cooperation between the AL and MT terms due to the inter-orbital nesting.

In contrast, the FO instability that corresponds to $\lambda_{\mathbf{0}}$ originates mostly from the AL term owing to the combination of $\chi_{3,3;3,3}^s(\mathbf{q})$ and $\chi_{3,3;3,3}^s(-\mathbf{q})$ for $\mathbf{q} \approx (\pi, 0)$, as discussed in Refs. [17, 18, 20].

Here, we explain that a pseudogap originates from the band-folding driven band-hybridization under the $\mathbf{q} = (0, \pi)$ AFB order. Since the form factor grows in proportion to $\text{Re}\sqrt{\lambda_{\mathbf{q}} - 1}$ in the Ginzburg-Landau theory, we introduce the mean-field-like T -dependent form factor $\hat{f}^{\mathbf{q}}(T) = f^{\text{max}} \tanh\left(1.74\sqrt{T^*/T - 1}\right) \hat{f}_{\text{DW}}^{\mathbf{q}}$, where $\hat{f}_{\text{DW}}^{\mathbf{q}}$ is the obtained form factor normalized as $\max_{\mathbf{k}} |f_{\text{DW}}^{\mathbf{q}}(\mathbf{k})| = 1$. We put $f^{\text{max}} = 60\text{meV}$. Details of calculation method under the AFB order are explained in SM B [45]. Figure 3(a) shows the obtained DOS. For $T < T^*$, a pseudogap appears, which is consistent with the ARPES measurement [38]. Figures 3(b) and 3(c) show the FSS and spectral weight, respectively un-

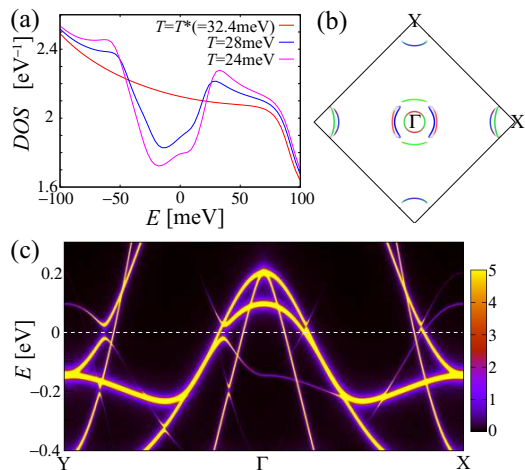


FIG. 3. (a) DOS at $T = T^* (= 32.4\text{meV})$, 28meV , and 24meV in the AFB state. Here, we introduced the quasiparticle damping $\gamma = 10\text{meV}$. (b) FSS and (c) spectral weight for $\gamma = 1\text{meV}$ under $\mathbf{q} = (0, \pi)$ AFB order at $T = 28\text{meV}$ in the original two-Fe Brillouin zone.

der the $\mathbf{q} = (0, \pi)$ AFB order at $T = 28\text{meV}$. Here, the folded band structure under the AFB order is unfolded to the original two-Fe Brillouin zone by following Ref. [50], which gives the spectrum corresponding to the ARPES measurements [38, 39, 51]. Owing to the band-folding, several Dirac-type bandstructures and shadow bands appear, as reported through an ARPES study [51].

In the following, we explain the “hidden nature” of the present AFB order, that is, the tiny anomalies in $\chi^s(\mathbf{Q})$ and $\chi_{\text{nem}}(\mathbf{0})$ at T^* . This is a long-standing mystery in Ba122. The T dependences of α_s with and without $f^{(0,\pi)}(T)$ are shown in Fig. S2 in SM B [45]. The AFB order suppresses α_s only slightly since the spin fluctuations are essentially intra-orbital, while intra-orbital components of $f^{(0,\pi)}(T)$ are sub-dominant. Next, we analyze the T dependencies of eigenvalue $\lambda_{\mathbf{q}}$ for the FO order and AFB order by following SM B [45]. As shown in Fig. 4 (a), the FO-order eigenvalue $\lambda_{\mathbf{0}}$ is suppressed only slightly by the finite AFB order, owing to the slight decrease of α_s and the “orbital selectivity” in nematicity: We stress that the dominant component of form factor is different between the off-diagonal $f_{3,4}^{(0,\pi)}$ in the AFB order and the diagonal $f_{3,3(4,4)}^{\mathbf{0}}$ ($f_{3,4}^{\mathbf{0}} = 0$) in the FO order as shown in SM C [45]. Thus, neither $\chi^s(\mathbf{Q}) \propto 1/(1 - \alpha_s)$ nor $\chi_{\text{nem}}(\mathbf{0}) \propto 1/(1 - \lambda_{\mathbf{0}})$ would show a visible anomaly at T^* , which is consistent with experiments. (Here, the increment of T_S due to the electron-phonon interaction is not considered for simplicity.) In contrast, the FO order at T_S causes a sizable anomaly for $\chi^s(\mathbf{Q})$ and $\chi_{\text{nem}}(\mathbf{0})$.

Another long-standing mystery is the T -linear behavior of nematicity ψ in Ba122 [34] and NaFeAs [40] below T^* . In order to solve this mystery, we calculate the T dependence of nematicity $\psi = (n_2 - n_3)/(n_2 + n_3)$ in

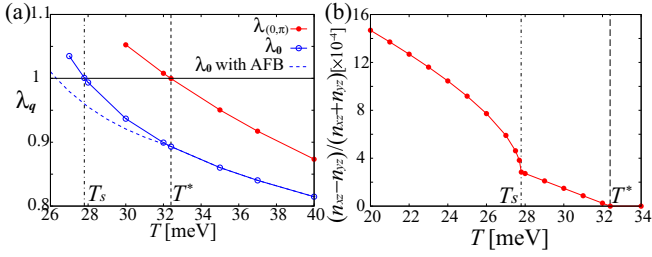


FIG. 4. (a) T dependencies of λ_q for $\mathbf{q} = (0, \pi)$ and $\mathbf{q} = \mathbf{0}$. The blue dotted line shows λ_0 with the AFB order for $T < T^*$. (b) The nematicity $\psi = (n_2 - n_3)/(n_2 + n_3)$ including both AFB order for $T < T^*$ and FO order for $T < T_S$.

Fig. 4(b), where both $\hat{f}^{(0, \pi)}(T)$ for $T < T^*$ and the FO order $\hat{f}^0(T)$ for $T < T_S$ are introduced. For $T < T_S$, we assume $\hat{f}^0(T) = f^{\max} \tanh(1.74\sqrt{T_S/T - 1}) \hat{f}_{\text{DW}}^0$, where \hat{f}_{DW}^0 is the obtained form factor normalized as $\max_{\mathbf{k}} |f_{\text{DW}}^0(\mathbf{k})| = 1$. Details of \hat{f}_{DW}^0 are presented in SM C [45]. We employ $f^{\max} = 60\text{meV}$, which corresponds to the energy split $\sim 60\text{meV}$ in the ARPES measurements [1]. Because the AFB order only slightly suppresses the FO-order transition as shown in Fig. 4(a), the obtained multistage nematic transitions are naturally expected in Ba122. The T -linear behavior $\psi \propto (T^* - T)$ for $T_S < T < T^*$ is a consequence of the relation $\psi \propto [f^{(0, \pi)}(T)]^2$ because the $f^{(0, \pi)}$ term cannot contribute to any $\mathbf{q} = \mathbf{0}$ linear response. Note that the form factor $\hat{f}^{(\pi, 0)}$ for $\mathbf{q} = (\pi, 0)$ gives $\psi < 0$. Thus, the T -linear behavior of ψ below T^* is also naturally explained by the AFB order. On the other hand, $\psi \propto \sqrt{T_S - T}$ for $T < T_S$ is induced by the FO order. To summarize, long-standing mysteries in the hidden-nematic phase, such as tiny anomalies in $\chi^s(\mathbf{Q})$ and $\chi_{\text{nem}}(\mathbf{0})$ at T^* and a T -linear ϕ below T^* , are naturally explained in the present AFB-order scenario.

Finally, we discuss the universality of the hidden nematic order by focusing on NaFeAs and FeSe. According to the ARPES measurement in NaFeAs [52, 53], only a single hole-band mainly composed of d_{xy} -orbital crosses the Fermi level, resulting from the spin-orbit interaction (SOI)-induced band hybridization. To reproduce the single d_{xy} -orbital-like hole-pocket in NaFeAs, we introduce the NaFeAs model without SOI by shifting downwards the d_{xz} and d_{yz} hole-bands immediately below the Fermi level in the BaFe₂As₂ model. The FSs in the NaFeAs model are shown in Fig. 5 (a). Details of the model are presented in SM A [45]. The obtained T dependencies of λ_q in Fig. 5 (b) is similar to that in the BaFe₂As₂ model. The AFB order in NaFeAs is naturally understood as a consequence of the inter-orbital nesting between h-FS3 and e-FSs, as we discussed above. The FO order is driven by the spin fluctuations on the d_{xz} and d_{yz} orbitals. They are not weak because the top of the d_{xz} and d_{yz} -orbital hole-band in NaFeAs is very close to

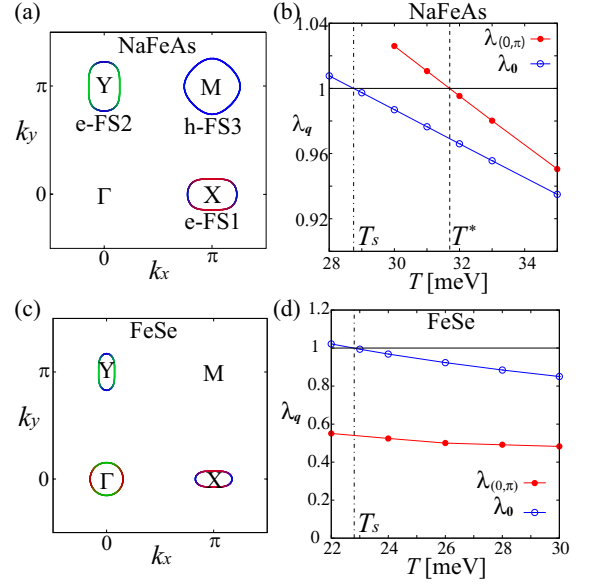


FIG. 5. (a) FSs of the NaFeAs model in the unfolded zone. (b) λ_q for $\mathbf{q} = (0, \pi)$ and $\mathbf{q} = \mathbf{0}$ in the NaFeAs model for $r = 0.339$ ($rU \sim 1.8\text{eV}$). Then, $\alpha_s = 0.92$ at $T = 30\text{meV}$. (c) FSs of the FeSe model. (d) λ_q in the FeSe model for $r = 0.239$ ($rU \sim 1.7\text{eV}$). Then, $\alpha_s = 0.85$ at $T = 30\text{meV}$.

the Fermi level according to the ARPES measurements [52, 53]. The derived multistage nematic transition is consistent with the experiment on NaFeAs [40]. On the other hand, the d_{xy} -orbital hole pocket is missing in the FeSe model shown in Fig. 5 (c). Because the inter-orbital nesting is missing, $\lambda_{(0, \pi)}$ in the FeSe model is considerably smaller than unity as shown in Figs. 5 (d) and S4 (b) in SM D [45], which is consistent with the absence of the hidden nematic order in FeSe [43].

In this numerical study, we neglected the self-energy. However, the results are essentially unchanged if the self-energy is incorporated into the DW equation, as we verified in SM E [45]: We incorporate the self-energy into the DW equation in the framework of the conserving approximation, where the macroscopic conservation laws are satisfied rigorously and unphysical results are avoided.

In summary, we demonstrated that the origin of the hidden nematic state for $T_S < T < T^*$ in BaFe₂As₂ and NaFeAs, which is a long-standing unsolved problem, is naturally explained as the AFB ordered state. The tiny T -linear nematicity $\psi = (n_{xz} - n_{yz})/(n_{xz} + n_{yz})$ as well as the emergence of the pseudogap and shadow band are naturally explained based on the present scenario. The phase diagrams of Ba122 and NaFeAs are understood by the present multistage nematic transition scenario. In contrast, the hidden nematic order is absent in FeSe because of the absence of the d_{xy} -orbital hole pocket.

Finally, we stress that the bond fluctuations significantly contribute to the pairing mechanism, as explained in SM F [45]. We will discuss this novel pairing mecha-

nism in detail in future publications.

We are grateful to Y. Yamakawa for useful discussions. This work was supported by Grants-in-Aid for Scientific Research from MEXT, Japan (No. JP19H05825, JP18H01175, and JP17K05543)

-
- [1] M. Yi, D. H. Lu, J.-H. Chu, J. G. Analytis, A. P. Sorini, A. F. Kemper, B. Moritz, S.-K. Mo, R. G. Moore, M. Hashimoto, W.-S. Lee, Z. Hussain, T. P. Devereaux, I. R. Fisher, and Z.-X. Shen, *Proc. Natl. Acad. Sci. U.S.A.* **108**, 6878 (2011).
- [2] M. Yoshizawa, D. Kimura, T. Chiba, S. Simayi, Y. Nakanishi, K. Kihou, C.-H. Lee, A. Iyo, H. Eisaki, M. Nakajima, and S. Uchida, *J. Phys. Soc. Jpn.* **81**, 024604 (2012).
- [3] A. E. Böhmer, P. Burger, F. Hardy, T. Wolf, P. Schweiss, R. Fromknecht, M. Reinecker, W. Schranz, and C. Meingast, *Phys. Rev. Lett.* **112**, 047001 (2014).
- [4] Y. Gallais, R. M. Fernandes, I. Paul, L. Chauviere, Y.-X. Yang, M.-A. Measson, M. Cazayous, A. Sacuto, D. Colson, and A. Forget, *Phys. Rev. Lett.* **111**, 267001 (2013).
- [5] Y. Hu, X. Ren, R. Zhang, H. Luo, S. Kasahara, T. Watashige, T. Shibauchi, P. Dai, Y. Zhang, Y. Matsuda, and Y. Li, *Phys. Rev. B* **93**, 060504(R) (2016).
- [6] R. M. Fernandes, L. H. VanBebber, S. Bhattacharya, P. Chandra, V. Keppens, D. Mandrus, M. A. McGuire, B. C. Sales, A. S. Sefat, and J. Schmalian, *Phys. Rev. Lett.* **105**, 157003 (2010).
- [7] R. M. Fernandes, E. Abrahams, and J. Schmalian, *Phys. Rev. Lett.* **107**, 217002 (2011).
- [8] F. Wang, S. A. Kivelson, and D.-H. Lee, *Nat. Phys.* **11**, 959 (2015).
- [9] R. Yu, and Q. Si, *Phys. Rev. Lett.* **115**, 116401 (2015).
- [10] J. K. Glasbrenner, I. I. Mazin, H. O. Jeschke, P. J. Hirschfeld, and R. Valenti, *Nat. Phys.* **11**, 953 (2015).
- [11] C. Fang, H. Yao, W.-F. Tsai, J. P. Hu, and S. A. Kivelson, *Phys. Rev. B* **77**, 224509 (2008).
- [12] R. M. Fernandes and A. V. Chubukov, *Rep. Prog. Phys.* **80**, 014503 (2017).
- [13] F. Krüger, S. Kumar, J. Zaanen, J. van den Brink, *Phys. Rev. B* **79**, 054504 (2009).
- [14] W. Lv, J. Wu, and P. Phillips, *Phys. Rev. B* **80**, 224506 (2009).
- [15] C.-C. Lee, W.-G. Yin, and W. Ku, *Phys. Rev. Lett.* **103**, 267001 (2009).
- [16] H. Kontani, T. Saito, and S. Onari, *Phys. Rev. B* **84**, 024528 (2011).
- [17] S. Onari and H. Kontani, *Phys. Rev. Lett.* **109**, 137001 (2012).
- [18] S. Onari, Y. Yamakawa, and H. Kontani, *Phys. Rev. Lett.* **112**, 187001 (2014).
- [19] S. Onari, Y. Yamakawa, and H. Kontani, *Phys. Rev. Lett.* **116**, 227001 (2016).
- [20] Y. Yamakawa, S. Onari and H. Kontani, *Phys. Rev. X* **6**, 021032 (2016).
- [21] S. Onari and H. Kontani, *Iron-Based Superconductivity*, (ed. P.D. Johnson, G. Xu, and W.-G. Yin, Springer-Verlag Berlin and Heidelberg GmbH & Co. K (2015)).
- [22] K. Jiang, J. Hu, H. Ding, and Z. Wang, *Phys. Rev. B* **93**, 115138 (2016).
- [23] L. Fanfarillo, G. Giovannetti, M. Capone, and E. Bascones, *Phys. Rev. B* **95**, 144511 (2017).
- [24] A. V. Chubukov, M. Khodas, and R. M. Fernandes, *Phys. Rev. X* **6**, 041045 (2016).
- [25] B. A. Frandsen, E. S. Bozin, H. Hu, Y. Zhu, Y. Nozaki, H. Kageyama, Y. J. Uemura, W.-G. Yin, and S. J. L. Billinge, *Nat. Commun.* **5**, 5761 (2014).
- [26] G. Zhang, J. K. Glasbrenner, R. Flint, I. I. Mazin, and R. M. Fernandes, *Phys. Rev. B* **95**, 174402 (2017).
- [27] H. Nakaoka, Y. Yamakawa, H. Kontani *Phys. Rev. B* **93**, 245122 (2016).
- [28] M. Tsuchiizu, K. Kawaguchi, Y. Yamakawa, and H. Kontani, *Phys. Rev. B* **97**, 165131 (2018).
- [29] J. Li, D. Zhao, Y. P. Wu, S. J. Li, D. W. Song, L. X. Zheng, N. Z. Wang, X. G. Luo, Z. Sun, T. Wu, and X. H. Chen, arXiv:1611.04694.
- [30] X. Liu, R. Tao, M. Ren, W. Chen, Q. Yao, T. Wolf, Y. Yan, T. Zhang, and D. Feng, *Nat. Commun.* **10**, 1039 (2019).
- [31] K. Ishida, M. Tsujii, S. Hosoi, Y. Mizukami, S. Ishida, A. Iyo, H. Eisaki, T. Wolf, K. Grube, H. v. Löhneysen, R. M. Fernandes, and T. Shibauchi, *Proc. Natl. Acad. Sci. USA* **117**, 6424 (2020).
- [32] S. Onari and H. Kontani, *Phys. Rev. B* **100**, 020507(R) (2019).
- [33] V. Borisov, R. M. Fernandes, and R. Valenti, *Phys. Rev. Lett.* **123**, 146402 (2019).
- [34] S. Kasahara, H. J. Shi, K. Hashimoto, S. Tonegawa, Y. Mizukami, T. Shibauchi, K. Sugimoto, T. Fukuda, T. Terashima, Andriy H. Nevidomskyy, and Y. Matsuda, *Nature* **486**, 382 (2012).
- [35] Y. K. Kim, W. S. Jung, G. R. Han, K.-Y. Choi, C.-C. Chen, T. P. Devereaux, A. Chainani, J. Miyawaki, Y. Takata, Y. Tanaka, M. Oura, S. Shin, A. P. Singh, H. G. Lee, J.-Y. Kim, and C. Kim, *Phys. Rev. Lett.* **111**, 217001 (2013).
- [36] E. Thewalt, I. M. Hayes, J. P. Hinton, A. Little, S. Patankar, L. Wu, T. Helm, C. V. Stan, N. Tamura, J. G. Analytis, and J. Orenstein, *Phys. Rev. Lett.* **121**, 027001 (2018).
- [37] T. Shimojima *al.*, unpublished.
- [38] T. Shimojima *et al.*, *Phys. Rev. B* **89**, 045101 (2014).
- [39] T. Shimojima, W. Malaeb, A. Nakamura, T. Kondo, K. Kihou, C.-H. Lee, A. Iyo, H. Eisaki, S. Ishida, M. Nakajima, S. Uchida, K. Ohgushi, K. Ishizaka, and S. Shin, *Sci. Adv.* **3**, e1700466 (2017).
- [40] R. Zhou, L. Y. Xing, X. C. Wang, C. Q. Jin, and G.-Q. Zheng, *Phys. Rev. B* **93**, 060502(R) (2016).
- [41] X. Ren, L. Duan, Y. Hu, J. Li, R. Zhang, H. Luo, P. Dai, and Y. Li, *Phys. Rev. Lett.* **115**, 197002 (2015).
- [42] H. Man, R. Zhang, J. T. Park, X. Lu, J. Kulda, A. Ivanov, and P. Dai, *Phys. Rev. B* **97**, 060507(R) (2018).
- [43] T. Shimojima, Y. Suzuki, T. Sonobe, A. Nakamura, M. Sakano, J. Omachi, K. Yoshioka, M. Kuwata-Gonokami, K. Ono, H. Kumigashira, A. E. Böhmer, F. Hardy, T. Wolf, C. Meingast, H. v. Löhneysen, H. Ikeda, and K. Ishizaka, *Phys. Rev. B* **90**, 121111(R) (2014).
- [44] H. Nakaoka, Y. Yamakawa, and H. Kontani, *Phys. Rev. B* **98**, 125107 (2018).
- [45] See Supplemental Material at URL for details of the models, formulation, tiny anomaly of α_s at T^* , form factor of FO order, FO order without mass-enhancement factor in FeSe, conserving approximation, and pairing interaction by the AFB fluctuations.

- [46] T. Miyake, K. Nakamura, R. Arita, and M. Imada, *J. Phys. Soc. Jpn.* **79**, 044705 (2010).
- [47] K. Kawaguchi, M. Tsuchiizu, Y. Yamakawa, and H. Kontani, *J. Phys. Soc. Jpn.* **86**, 063707 (2017).
- [48] Y. Yamakawa and H. Kontani, *Phys. Rev. Lett.* **114**, 257001 (2015).
- [49] R. Q. Xing, L. Classen, A. V. Chubukov, *Phys. Rev. B* **98**, 041108(R) (2018).
- [50] W. Ku, T. Berlijn, and C.-C. Lee, *Phys. Rev. Lett.* **104**, 216401 (2010).
- [51] A. Fujimori, private communication.
- [52] M. Yi, D. H. Lu, R. G. Moore, K. Kihou, C.-H. Lee, A. Iyo, H. Eisaki, T. Yoshida, A. Fujimori, and Z.-X. Shen, *New J. Phys.* **14**, 073019 (2012).
- [53] M. D. Watson, S. Aswartham, L. C. Rhodes, B. Parrett, H. Iwasawa, M. Hoesch, I. Morozov, B. Büchner, and T. K. Kim *Phys. Rev. B* **97**, 035134 (2018).

[Supplementary Material]

Hidden antiferro-nematic order in Fe-based superconductor BaFe₂As₂ and NaFeAs above T_S

Seiichiro Onari and Hiroshi Kontani

Department of Physics, Nagoya University, Nagoya 464-8602, Japan

A: Eight-orbital models for BaFe₂As₂ and FeSe

Here, we introduce the eight-orbital d - p models for BaFe₂As₂, FeSe, and NaFeAs that are analyzed in the main text. We first derive first-principles tight-binding models by using the WIEN2k [1] and WANNIER90 [2] codes. The model for BaFe₂As₂ is directly given by the first-principles tight-binding model without any modification.

Next, to obtain the experimentally observed Fermi surfaces (FSs) in FeSe, we introduce the k -dependent shifts for orbital l , δE_l , by introducing the intra-orbital hopping parameters, as explained in Ref. [3]. We shift the d_{xy} -orbital band [$d_{xz/yz}$ -orbital band] at (Γ , M, X) points by $(-0.6\text{eV}, -0.25\text{eV}, +0.24\text{eV})$ [$(-0.24\text{eV}, 0\text{eV}, +0.12\text{eV})$] for FeSe. The NaFeAs model is constructed by shifting the $d_{xz/yz}$ -orbital band of the BaFe₂As₂ model at Γ point by -0.3eV in order to reproduce the experimental FSs of NaFeAs without the SOI.

We also introduce the mass-enhancement factor $z^{-1} = 1.6$ for the d_{xy} orbital in FeSe, while $z^{-1} = 1$ for other orbitals.

Figure S1 shows the bandstructures of the obtained BaFe₂As₂ model, FeSe model, and NaFeAs model.

Here, we explain the d -orbital Coulomb interaction introduced by the constraint RPA (cRPA) method for each compound in Ref. [4]. The Coulomb interaction for the spin channel in the main text is

$$(\Gamma^s)_{l_1 l_2, l_3 l_4} = \begin{cases} U_{l_1, l_1}, & l_1 = l_2 = l_3 = l_4 \\ U'_{l_1, l_2}, & l_1 = l_3 \neq l_2 = l_4 \\ J_{l_1, l_3}, & l_1 = l_2 \neq l_3 = l_4 \\ J_{l_1, l_2}, & l_1 = l_4 \neq l_2 = l_3 \\ 0, & \text{otherwise.} \end{cases} \quad (\text{S1})$$

Furthermore, the Coulomb interaction for the charge channel is

$$(\hat{\Gamma}^c)_{l_1 l_2, l_3 l_4} = \begin{cases} -U_{l_1, l_1}, & l_1 = l_2 = l_3 = l_4 \\ U'_{l_1, l_2} - 2J_{l_1, l_2}, & l_1 = l_3 \neq l_2 = l_4 \\ -2U'_{l_1, l_3} + J_{l_1, l_3}, & l_1 = l_2 \neq l_3 = l_4 \\ -J_{l_1, l_2}, & l_1 = l_4 \neq l_2 = l_3 \\ 0, & \text{otherwise.} \end{cases} \quad (\text{S2})$$

The averaged intra-orbital Coulomb interaction is 5.2eV and 7.2eV for BaFe₂As₂ and FeSe compounds, respectively [4].

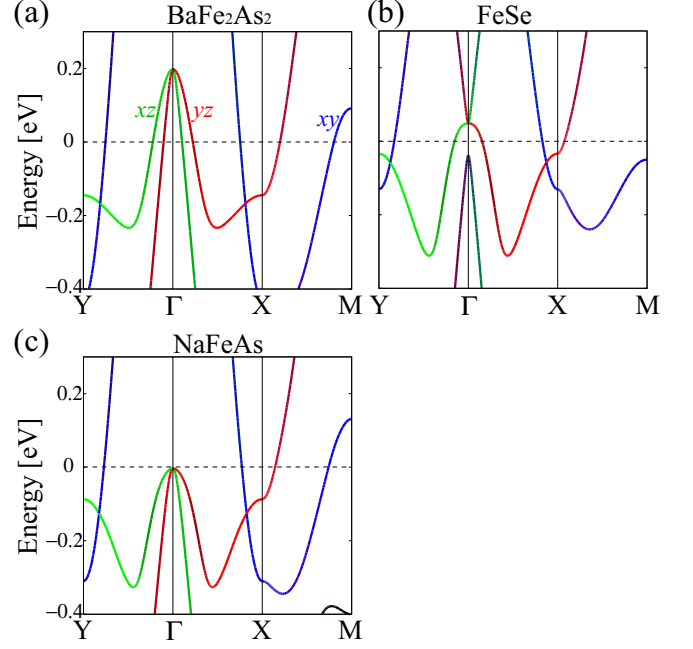


FIG. S1. Obtained bandstructures of (a) the BaFe₂As₂ model, (b) FeSe model, and (c) NaFeAs model.

By using the multiorbital Coulomb interaction, the spin (charge) susceptibility in the RPA is given by

$$\hat{\chi}^{s(c)}(q) = \hat{\chi}^0(q)[1 - \hat{\Gamma}^{s(c)}\hat{\chi}^0(q)]^{-1}, \quad (\text{S3})$$

where the irreducible susceptibility is

$$\chi_{l,l';m,m'}^0(q) = -\frac{T}{N} \sum_k G_{l,m}(k+q)G_{m',l'}(k). \quad (\text{S4})$$

Here, $\hat{G}(k)$ is the multiorbital Green function introduced in the main text.

The kernel function $\hat{K}^q(k, k')$ [5, 6] is given by

$$K_{l,l';m,m'}^q(k, k') = - \sum_{m_1, m_2} I_{l,l';m_1, m_2}^q(k, k') g_{m_1, m_2; m, m'}^q(k'), \quad (\text{S5})$$

where $g_{l,l';m,m'}^q(k) \equiv G_{l,m}(k+q)G_{m',l'}(k)$, and $\hat{I}^q(k, k')$ is the four-point vertex.

$\hat{I}^q(k, k')$ is given as

$$I_{l,l';m,m'}^q(k, k') = \sum_{b=s,c} \left[-\frac{a^b}{2} V_{l,m;l',m'}^b(k-k') \right]$$

$$\begin{aligned}
& + \frac{T}{N} \sum_{p,l_1,l_2,m_1,m_2} \frac{a^b}{2} V_{l,l_1;m,m_2}^b(p+\mathbf{q}) V_{m',l_2;l',m_1}^b(p) \\
& \quad \times G_{l_1,m_1}(k-p) G_{l_2,m_2}(k'-p) \\
& + \frac{T}{N} \sum_{p,l_1,l_2,m_1,m_2} \frac{a^b}{2} V_{l,l_1;l_2,m'}^b(p+\mathbf{q}) V_{m_2,m;l',m_1}^b(p) \\
& \quad \times G_{l_1,m_1}(k-p) G_{l_2,m_2}(k'+p+\mathbf{q}), \quad (\text{S6})
\end{aligned}$$

where $a^s = 3$, $a^c = 1$, $p = (\mathbf{p}, \omega_l)$, and $\hat{V}^{s(c)}(\mathbf{q}) = \hat{\Gamma}^{s(c)} + \hat{\Gamma}^{s(c)} \hat{\chi}^{s(c)}(\mathbf{q}) \hat{\Gamma}^{s(c)}$.

In Eq. (S6), the first line corresponds to the Maki-Thompson (MT) term, and the second and third lines give the AL1 and AL2 terms, respectively. In the MT term, the first-order term with respect to $\hat{\Gamma}^{s,c}$ gives the Hartree-Fock (HF) term in the mean-field theory.

B: Tiny anomaly of α_s at T^*

Here, we analyze the T dependence of α_s with and without AFB order $\hat{f}^{(0,\pi)}(T)$. The AFB order $\hat{f}^{(0,\pi)}(T)$ gives modulation of the correlated hopping with period 2 along the y direction shown in Fig. 2 (c), which requires two times larger unit cell. By analyzing the Hamiltonian in the two times larger unit cell, we obtain a pseudogap due to the band-folding driven band-hybridization. We calculate the spin susceptibilities in the two times larger unit cell. As shown in Fig. S2, the AFB order suppresses α_s only slightly below T^* since the diagonal component of form factor, which mainly affect the value of α_s , is sub-dominant as mentioned below. Thus, the tiny anomalies in $\chi^s(\mathbf{Q}) \propto \frac{1}{1-\alpha_s}$ at T^* , which is a long-standing mystery in Ba122, is naturally explained by the AFB order.

By using the spin susceptibilities in the two times larger unit cell, we develop the method of DW equation under the AFB order, which is complicated and heavy numerical calculation.

In the main text, the dominant form factor is $f_{3,4}^{(0,\pi)}$ shown in Fig. 2(b). $f_{4,4}^{(0,\pi)}$ and $f_{3,3}^{(0,\pi)}$ also emerge as the sub-dominant form factors, which correspond to the intra-orbital AFB order with the modulation of correlation hopping $\pm\delta t$ with period 2 along the y direction.

The single-component GL theory considering terms up to the sixth order in Ref. [7] leads to the prediction that the second-order transition at $T = T^*$ and the meta-nematic transition at $T = T_S$. In the present theory, in contrast, both transitions are second-order owing to the multiorbital component of the form factor. In addition, the T -linear dependence of ψ for $T_S < T < T^*$ is naturally explained by the AFB order in our theory.

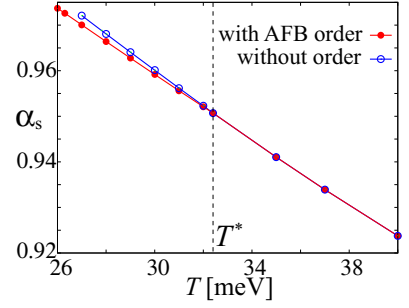


FIG. S2. T dependencies of α_s with and without the AFB order.

C: Form factor of FO order

Here, we explain the obtained $\mathbf{q} = \mathbf{0}$ form factor in BaFe₂As₂. Figures S3 (a) and (b) show the dominant form factors for $\mathbf{q} = \mathbf{0}$. $f_{4,4}^{\mathbf{0}} \propto \cos k_x - \cos k_y$ corresponds to the B_{1g} bond order of orbital 4 as shown in Fig. S3 (c). Figure S3 (b) shows $f_{3,3}^{\mathbf{0}}(k_x, k_y) = -f_{2,2}^{\mathbf{0}}(-k_y, k_x)$, which causes the B_{1g} FO order $n_2 > n_3$ in Fig. S3 (d). The off-diagonal $f_{3,4}^{\mathbf{0}}$ is 0, while the $f_{3,4}^{(0,\pi)}$ is dominant in the AFB order. Note that the $f_{3,3}^{\mathbf{0}}$ gives sign reversal orbital order (OO), which is consistent with ARPES measurements in FeSe, Ba122 and La1111 [8–10].

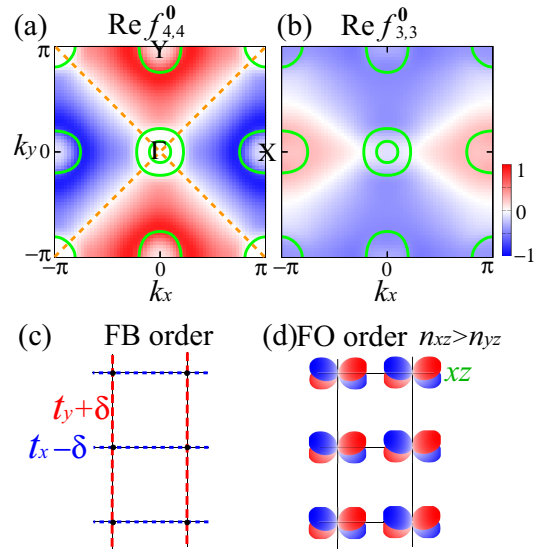


FIG. S3. Form factors at $\mathbf{q} = \mathbf{0}$ obtained as the second-largest eigenvalue in the BaFe₂As₂ model on (a) orbital 4 and (b) orbital 3. The green lines denote FSs without the self-energy. The form factor for orbital 4, $f_{4,4}^{\mathbf{0}} \propto \cos k_x - \cos k_y$, results in the ferro-bond (FB) order. Schematic pictures of (c) FB order due to $f_{4,4}^{(0,\pi)}$ and (d) FO order due to $f_{3,3}^{(0,2,2)}$.

D: Results in FeSe model

In the FeSe model employed in main text, we put the mass-enhancement factor $z^{-1} = 1.6$ for d_{xy} orbital by following Ref. [5]. Here, we show that the qualitative results do not depend on the value of z by calculating the case of $z = 1$ (without any mass-enhancement factor) in the FeSe model.

Figure S4 (a) shows \mathbf{q} dependence of $\lambda_{\mathbf{q}}$ at $T = 30\text{meV}$ in the FeSe model for $z = 1$. We see that the $\mathbf{q} = \mathbf{0}$ FO order dominates over $\mathbf{q} = (0, \pi)$ AFB order. This result is confirmed by the T -dependences of $\lambda_{\mathbf{q}}$ for $\mathbf{q} = (0, \pi)$ and $\mathbf{q} = \mathbf{0}$ shown in Fig. S4 (b), which are similar to the results in main text for $z^{-1} = 1.6$ shown in Fig. 5 (d). Thus, AFB order is absent in the FeSe model even for $z = 1$. The qualitative results do not depend on the value of z .

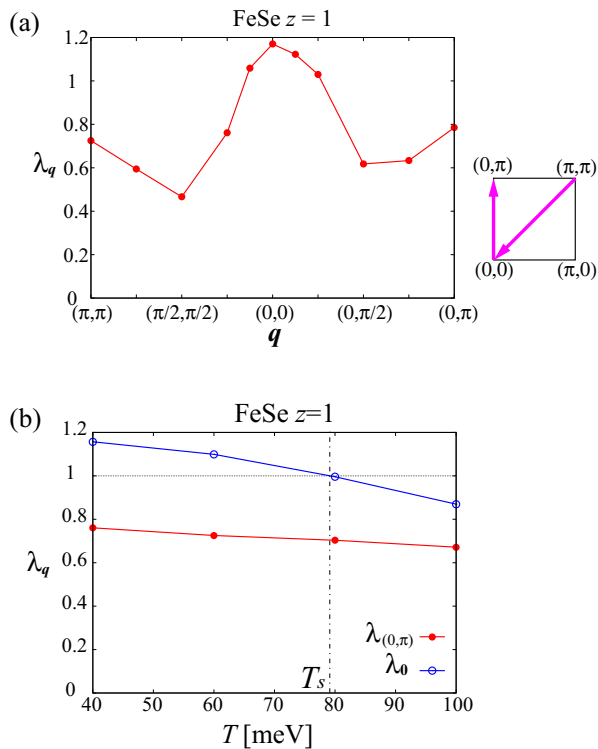


FIG. S4. (a) Obtained \mathbf{q} dependence of $\lambda_{\mathbf{q}}$ at $T = 30\text{meV}$ in the FeSe model for $z = 1$ and $r = 0.221$ ($rU \sim 1.6\text{eV}$). Then, $\alpha_s = 0.85$ at $T = 30\text{meV}$. The \mathbf{q} path is shown by arrows in the right panel. (b) T -dependences of $\lambda_{\mathbf{q}}$ for $\mathbf{q} = (0, \pi)$ and $\mathbf{q} = \mathbf{0}$ in the FeSe model for $z = 1$ and $r = 0.221$.

E: Conserving approximation

In the main text, we employ the RPA, in which the self-energy is not included in the spin (charge) susceptibility $\hat{\chi}^{s(c)}$ and kernel function $\hat{K}^{\mathbf{q}}(k, k')$. For this reason, the DW equation in the RPA violates the conserving-

approximation (CA) formalism of Baym and Kadanoff [11, 12]. The great merit of CA is that it rigorously satisfies the macroscopic conservation laws. This merit is important to avoid unphysical results. Here, we first calculate the one-loop self-energy by using the fluctuation exchange (FLEX) approximation [5, 13]. Next, we solve the DW equation including the FLEX self-energy to satisfy the CA formalism.

The FLEX self-energy (C_4) is given by $\hat{\Sigma}(k) = \frac{T}{N} \sum_q \hat{V}^{\Sigma}(q) \hat{G}(k-q)$, where $\hat{G}(k) = [(i\epsilon_n - \mu)\hat{1} - \hat{h}^0(\mathbf{k}) - \hat{\Sigma}(k)]^{-1}$ is the Green function with the self-energy, and \hat{V}^{Σ} is the interaction matrix for the self-energy. \hat{V}^{Σ} is given as

$$\begin{aligned} \hat{V}^{\Sigma} = & \frac{3}{2} \hat{\Gamma}^s \hat{\chi}^s(q) \hat{\Gamma}^s + \frac{1}{2} \hat{\Gamma}^c \hat{\chi}^c(q) \hat{\Gamma}^c \\ & - \frac{1}{2} \left[\hat{\Gamma}^c \hat{\chi}^0(q) \hat{\Gamma}^c + \hat{\Gamma}^s \hat{\chi}^0(q) \hat{\Gamma}^s \right. \\ & \left. - \frac{1}{4} (\hat{\Gamma}^s + \hat{\Gamma}^c) \hat{\chi}^0(q) (\hat{\Gamma}^s + \hat{\Gamma}^c) \right]. \end{aligned} \quad (\text{S7})$$

We solve $\hat{\Sigma}$, \hat{G} , and $\hat{\chi}^{s(c)}$ self-consistently. The effect of the renormalization factor z is given by the self-energy $\hat{\Sigma}$ in this framework. By introducing the obtained functions, we improve the kernel of the DW equation in Eq. (S5) and (S6) and solve the symmetry-breaking self-energy (form factor) in the framework of CA.

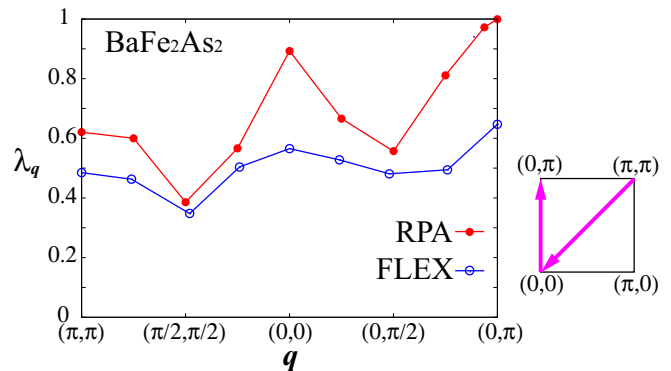


FIG. S5. \mathbf{q} dependences of $\lambda_{\mathbf{q}}$ obtained using the RPA at $T = T^*$ ($\alpha_s = 0.951$) and the FLEX approximation at $T = 5\text{meV}$ ($\alpha_s = 0.945$) in the BaFe_2As_2 model. The \mathbf{q} path is shown by arrows in the right panel.

Figure S5 shows the \mathbf{q} dependences of $\lambda_{\mathbf{q}}$ obtained using the RPA at $T = T^* = 32.4\text{meV}$ (spin Stoner factor $\alpha_s = 0.951$) and the FLEX approximation at $T = 5\text{meV}$ ($\alpha_s = 0.945$, $r = 0.680$). The parameter α_s is a univariate function of the reduction parameter r in Eq. (1), and $1 - \alpha_s$ represents the distance from the magnetic critical point. In the numerical study, we take $N = 100 \times 100$ \mathbf{k} -meshes and 1024 Matsubara frequencies. The obtained mass-enhancement factor $z^{-1} = m^*/m \sim 5$ by the self-energy is consistent with experimental value. The result of the FLEX approximation is similar to that of RPA

employed in the main text. The AFB order $f^{(0,\pi)}$ is dominant over the FO order f^0 . Thus, the results in the main text are verified in the CA framework. The obtained value $\lambda_{(0,\pi)} \sim 0.6$ in the CA is still large, and it will reach unity for larger r or at lower T .

F: Pairing interaction by the AFB fluctuations

Here, we discuss the mechanism of superconductivity. In our previous paper [14], we proposed the mechanism by which the s_{++} -wave is mediated by AF orbital (AFO) fluctuations. Therein, we employed the \mathbf{k} -independent form factor $\hat{f}^{\mathbf{q}}(\mathbf{k}) = \hat{O}_{\Gamma}$ ($\Gamma = xz, yz, xy$), where \hat{O}_{Γ} is the local charge quadrupole operator. The obtained form factor in the main text is mainly the \mathbf{k} -dependent AFB order, which is different from the AFO order.

In the following, we show that the s_{++} -wave is realized because of the AFB fluctuations by using the \mathbf{k} -dependent and \mathbf{q} -dependent form factor obtained microscopically from the DW equation. The pairing interaction \hat{V}^{DW} originating from the DW susceptibility $\chi_{\text{nem}}(\mathbf{q}) \propto (1 - \lambda_{\mathbf{q}})^{-1}$ [15] is expanded by the form factor as

$$V_{l,l';m,m'}^{\text{DW}}(k, k') = \sum_{\mathbf{q}=0,\mathbf{Q},\mathbf{Q}'} f_{l,l'}^{\mathbf{q}}(\mathbf{k}') \frac{\alpha^{\mathbf{q}}}{1 + \xi_{\mathbf{q}}^2(\mathbf{k} - \mathbf{k}' - \mathbf{q})^2} f_{m,m'}^{\mathbf{q}*}(-\mathbf{k}' - \mathbf{q}) \quad (\text{S8})$$

where $\mathbf{Q} = (0, \pi)$, $\mathbf{Q}' = (\pi, 0)$, $\alpha^{\mathbf{q}} = \bar{I}^{\mathbf{q}}/(1 - \lambda_{\mathbf{q}})$, and $\xi_{\mathbf{q}}$ denotes the correlation length for the DW state with wave vector \mathbf{q} . We put $\xi_{\mathbf{q}} = 1.0$. $\bar{I}^{\mathbf{q}}$ is the mean value of $\hat{I}^{\mathbf{q}}$ in the basis of $\hat{f}^{\mathbf{q}}(\mathbf{k})$ at the lowest Matsubara frequency. It is given as

$$\bar{I}^{\mathbf{q}} = \frac{\sum_{\mathbf{k}, \mathbf{k}'} \sum_{l,l',m,m'} f_{l,l'}^{\mathbf{q}*}(\mathbf{k}) I_{l,l';m,m'}^{\mathbf{q}}(\mathbf{k}, \mathbf{k}') f_{m,m'}^{\mathbf{q}}(\mathbf{k}')}{\left[\sum_{\mathbf{k}} \sum_{l,l'} |f_{l,l'}^{\mathbf{q}}(\mathbf{k})|^2 \right]^2} \quad (\text{S9})$$

We obtain $\bar{I}^0 \sim 9\text{eV}$ in the BaFe_2As_2 model. Because of the large $\bar{I}^{\mathbf{q}}/U \sim 6$, the AFB fluctuations yield a large attractive pairing interaction. The obtained enhancement of $\bar{I}^{\mathbf{q}}$ is consistent with the large charge-channel U-VC at low energies in the beyond-Migdal-Eliashberg theory in Refs. [16, 17]. We solve the following Eliashberg equation, which includes the RPA pairing interaction and the DW fluctuation pairing interaction \hat{V}^{DW} with the cutoff energy $W_c = 0.02\text{eV}$:

$$\lambda_{\text{SC}} \Delta_{l,m}(k) = \frac{T}{N} \sum_{k'} \sum_{l',l'',m',m''} \left[-\frac{3}{2} \hat{V}^s(k - k') + \frac{1}{2} \hat{V}^c(k - k') + \hat{V}^{\text{DW}}(k, k') + \frac{1}{2} (\hat{\Gamma}^c - \hat{\Gamma}^s) \right]_{l,l';m',m} \times G_{l',l''}(k') G_{m',m''}(-k') \Delta_{l'',m''}(k'). \quad (\text{S10})$$

In order to concentrate on the FSs, we define θ as the azimuthal angle θ with respect to the x axis on each FS

shown in Fig. S6(a). Figure S6(b) shows the derived s_{++} -wave gap function Δ as a function of the θ on each FS. We find that the fullgap s_{++} wave is obtained because the obtained AFB fluctuations with large inter and intra (2–4) orbital components yield a sizable inter-FS attractive pairing interaction. Thus, we find that the AFB fluctuations with a non-local form factor is a novel mechanism of the s_{++} wave. The present AFB-fluctuation mechanism is a natural extension of the beyond-Migdal-Eliashberg theory with U-VC developed in Refs. [16, 17]. In future publications, we will discuss the details of results and the mechanism of superconductivity based on the DW fluctuations.

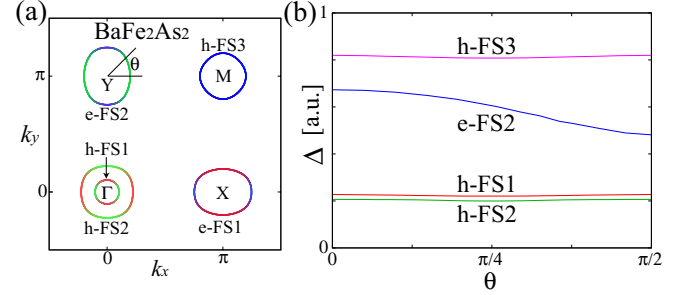


FIG. S6. (a) FSs of the BaFe_2As_2 model in the unfolded zone, where θ denotes the azimuthal angle with respect to the x axis on each FS. (b) Superconducting gap function at $T = 30\text{meV}$ given by the DW fluctuations as a function of θ .

- [1] P. Blaha, K. Schwarz, G. Madsen, D. Kvasnicka, J. Luitz, R. Laskowski, F. Tran, and L. Marks, wien2k: An Augmented Plane Wave plus Local Orbitals Program for Calculating Crystal Properties (Vienna University of Technology, 2018).
- [2] AA Mostofi, JR Yates, G Pizzi, YS Lee, I Souza, D Vanderbilt, N Marzari, Comput. Phys. Commun. **185**, 2309 (2014).
- [3] Y. Yamakawa, S. Onari and H. Kontani, Phys. Rev. X **6**, 021032 (2016).
- [4] T. Miyake, K. Nakamura, R. Arita, and M. Imada, J. Phys. Soc. Jpn. **79**, 044705 (2010).
- [5] S. Onari, Y. Yamakawa, and H. Kontani, Phys. Rev. Lett. **116**, 227001 (2016).
- [6] K. Kawaguchi, M. Tsuchiizu, Y. Yamakawa, and H. Kontani, J. Phys. Soc. Jpn. **86**, 063707 (2017).
- [7] S. Kasahara, H. J. Shi, K. Hashimoto, S. Tonegawa, Y. Mizukami, T. Shibauchi, K. Sugimoto, T. Fukuda, T. Terashima, Andriy H. Nevidomskyy, and Y. Matsuda, Nature **486**, 382 (2012).
- [8] Y. Suzuki, T. Shimojima, T. Sonobe, A. Nakamura, M. Sakano, H. Tsuji, J. Omachi, K. Yoshioka, M. Kuwata-Gonokami, T. Watashige, R. Kobayashi, S. Kasahara, T. Shibauchi, Y. Matsuda, Y. Yamakawa, H. Kontani, and K. Ishizaka, Phys. Rev. B **92**, 205117 (2015).
- [9] H. Pfau, C. R. Rotundu, J. C. Palmstrom, S. D. Chen,

- M. Hashimoto, D. Lu, A. F. Kemper, I. R. Fisher, Z.-X. Shen, Phys. Rev. B **99**, 035118 (2019).
- [10] S. S. Huh, Y. S. Kim, W. S. Kyung, J. K. Jung, R. Kappenberger, S. Aswartham, B. Büchner, J. M. Ok, J. S. Kim, C. Dong, J. P. Hu, S. H. Cho, D. W. Shen, J. D. Denlinger, Y. K. Kim, and C. Kim, arXiv:2003.10618.
- [11] G. Baym and P. Kadanoff, Phys. Rev. **124**, 287 (1961).
- [12] S. Allen, A.-M. S. Tremblay, and Y. M. Vilk, *Theoretical Methods for Strongly Correlated Electrons*, Eds. D. Senechal, A.-M. Tremblay, C. Bourbonnais (Springer-Verlag, New-York, 2004).
- [13] N. E. Bickers and S. R. White, Phys. Rev. B **43**, 8044 (1991).
- [14] H. Kontani, T. Saito, and S. Onari, Phys. Rev. B **84**, 024528 (2011).
- [15] S. Onari and H. Kontani, Phys. Rev. B **100**, 020507(R) (2019).
- [16] S. Onari, Y. Yamakawa, and H. Kontani, Phys. Rev. Lett. **112**, 187001 (2014).
- [17] R. Tazai and H. Kontani, Phys. Rev. B **98**, 205107 (2018).